Rev.Adv.Mater.Sci. 16(2007) 51-72

DEVELOPMENT AND APPLICATION OF THE DISLOCATION MODEL FOR ANALYSIS OF THE MICROSTRUCTURE EVOLUTION AND DEFORMATION BEHAVIOR OF METALS SUBJECTED TO SEVERE PLASTIC DEFORMATION

I. V. Alexandrov and R. G. Chembarisova

Department of Physics, Ufa State Aviation Technical University, 12 K. Marx St., Ufa, 450000, Russia

Received: April 17, 2007

Abstract. The upgraded Estrin-Tóth model is presented to describe the deformation behavior of the materials subjected to severe plastic deformation. The model has been applied toward study of tension of the as-received Cu samples and the samples after the 1st, 4th, and 8th equal channel angular pressing passes. The dislocation density evolution in the two phases, namely in the boundaries of fragments/cell blocks and interiors, is studied. The evolution of the concentration of vacancies that formed during deformation, annihilation of dislocations during their non-conservative motion and generation of dislocations during multiple cross slip are considered. As a result, peculiarities of the microstructure evolution, causes of achieving high values of the vacancy concentrations and dislocation densities are revealed. Features of the deformation behavior of the considered samples are explained.

1. INTRODUCTION

It is well known that considerable microstructure refinement and, as a consequence, change of mechanical properties of metals takes place as a result of large plastic strains [1-3]. Low-angle boundaries that separate cells and blocks of cells are typical for such structures; they are also characterized by enhanced strength and low ductility.

The investigations of recent years have shown that the severe plastic deformation (SPD) leads to formation of ultrafine-grained (UFG) structures (grain size d less than 1 μm) and even nanostructured (d <100 nm) states with mainly high-angle grain boundaries [4]. SPD implies large plastic deformations (e>1) realized under high applied pressures of several GPa [4]. These structures may be characterized not only by high strength but also high ductility (SPD paradox) [5], low-temperature and/or high-rate superplasticity [6], absence of strain hardening (stages IV and V of strain hardening) [7].

High pressure torsion (HPT) and equal-channel angular pressing (ECAP) are main techniques for receiving bulk UFG and nanostructured states in different metallic materials [4]. The conducted experiments showed that the yield stress of the UFG Cu processed by SPD is several times higher than that of the conventional coarse-grained Cu before SPD. The strain hardening is insignificant at the plastic flow stage, as compared to the annealed coarse-grained state [8]. It is stated that not only the grain size but also the defect structure of grain boundaries influence the strength properties of Cu and other metals [8]. SPD Cu may have a relatively low [9] or high ductility [5] during tensile testing. This depends on the predominance of low-angle or high-angle grain boundaries in the structures formed at definite ECAP modes.

Corresponding author: I. V. Alexandrov, e-mail : iva@mail.rb.ru

As follows from the experiments [10], the average dislocation density in grains increases with the strain up to ~ 10^{15} m^{-2} after SPD of Cu. Meanwhile, the dislocation density is much higher in grain boundaries. At the same time, the average dislocation density can change non-monotonously, with the strain degree rising [11]. At that, the boundaries preserve their non-equilibrium state [10]. The intragranular slip makes a large contribution into the total strain. Similar results are observed in case of SPD of other metals and alloys [12,13].

Unusual mechanical properties are conditioned by the peculiarities of structure and processes, which accompany the deformation of UFG and nanostructured materials. Though intragranular slip is the main deformation mechanism for these materials, the dislocation accumulation observed in the grain body is not significant [4]; dislocations are presumably captured by grain boundaries. Increased diffusion is typical for grain boundaries in the UFG Cu [14]. It contributes to the recovery process during deformation of the UFG Cu at room temperature [4]. The activation energy of the grain boundary diffusion of ~ 79.2 kJ/mole in the UFG Cu is much lower than the value 107 kJ/mole typical for diffusion along the stationary grain boundaries in the coarse-grained Cu [4]. Absence of the dislocation accumulation may be also caused by activation of the recovery processes, which take place partially by means of the dislocation cross slip [15].

A high value of the yield stress, at which the condition the onset of plastic deformation is fulfilled, may be explained by an increase in the dislocation density during ECAP. Since any significant dislocation accumulation is not observed in the grain body, the origin of a high value of the yield stress is explained by the model based on the dislocation curvature mechanism [16]. Shortening of dislocation spacing in the grain boundaries leads to the stress growth. A high value of the stress is necessary for a Frank-Read source to start working in the boundary.

Equilibrium between the strain hardening and recovery in the grain boundaries takes place at the steady deformation stage [10]. The flow stress is controlled by nucleation of new dislocations at this stage. The results obtained in [6,17] show that the mechanical behavior of the UFG metals and alloys is determined by the dislocation substructure that formed during SPD.

The study of the mechanisms of unusual deformation behavior of SPD UFG and especially nanomaterials is of great scientific interest due to the peculiarities of the acting deformation mechanisms. Various models are used to analyze the strain hardening during plastic deformation. The simplest of them are the well-known Kocks-Mecking-Estrin models, which involve just one inner variable - the total dislocation density [18,19]. These models give a very good explanation to stage III of the strain hardening. S. Kok, A.J. Beaudoin, and D.A. Tortorelly [20] proposed a two-parameter model of hardening to describe stage IV of the strain hardening. The model is a further development of the Kocks-Mecking theory [19]. The latter consists in consideration of the density of geometrically necessary dislocations (GND).

Most of the models describing stage IV of the strain hardening assume that a sample may be considered as a two-phase composite material which consists of cell walls with a high dislocation density and interiors (cell bodies) with a low dislocation density. A three-parameter model proposed by Y. Estrin, L.S. Tóth, and others [21] relates to such models. The model enables describing stages III, IV, and V of the strain hardening within one single formalism. A three-parameter approximation was proposed by E. Nes and K. Marthinsen [22,23] during the simulation of the deformation behavior of metals. Their composite model describes the microstructure evolution. It is supposed that during small strains (stage II of the strain hardening) dislocations form a cell structure, which is characterized by the cell size δ and the wall thickness h, the dislocation density in the walls ρ_b and that in the interiors ρ_i. During large strains (stage IV of the strain hardening) misorientations between subboundaries are accounted for.

The models by M. Zehetbauer [24] and M. Zehetbauer and P. Les [25], which are based on Mughrabi's concept about the two-phase structure of dislocation cells [26], refer to the models which describe stages IV and V of the strain hardening. At that, the cell interior size L_1 and the cell wall thickness L_2 are used as structural parameters. According to the model by M. Zehetbauer [24], a cell body has screw dislocations which are located in cell interiors. The density of these dislocations is equal to ρ_1. Edge dislocations with the density ρ_2 are concentrated in the cell walls. The model accounts for the role of vacancies which create conditions for climb and annihilation of edge dislocations. The correspondence between the modeling and experimental data was shown in [27].

The presented models form a hierarchy of models depending on the number of the parameters used. The first three stages of the strain hardening

are controlled by one parameter. The number of the parameters should be increased up to three to describe stages IV and V of the strain hardening. The models which consider the occurrence of stages IV and V of the strain hardening as a result of the structural changes and the evolution of crystallographic texture are of great interest in case of SPD.

The analysis shows that the Estrin-Tóth model is one of the most developed strain hardening models [21,28]. Up to the present, the strain hardening curves which correspond to different deformation modes have been analyzed with the help of this model [28]. A visco-plastic self-consistent (VPSC) model [29] of polycrystal ductility is combined with the model to consider the crystallographic texture evolution. The dislocation densities in the cell walls ρ_w and interiors ρ_c are used as modeling parameters. The relation between the average dislocation density and the cell size is defined. The law of variation of the cell wall volume fraction against the strain degree is made. Stages IV and V of the strain hardening in fcc polycrystals are adequately modeled. The evolution character of the average dislocation density is predicted. The obtained results agree well with the experimental data. The model was also used to analyze the deformation behavior of the materials processed by severe plastic deformation [30].

In recent years special attention has been paid to revelation of the causes of formation of unusual mechanical properties in SPD nanostructured (NS) materials with a grain size less than 100 nm. Some deformation mechanisms such as emission of partial dislocations from grain boundaries and formation of stacking fault and twins were predicted on the basis of the molecular-dynamic modeling and observed experimentally [31,32].

A mechanical model of the deformation behavior of NS metals based on the assumption about the emission of partial dislocations from grain boundaries was developed by Asaro *et al*. [33]. It was shown that the stress required for the emission of partial dislocations is much lower than the stress required for the emission of total dislocations when the grain size becomes smaller than some critical value. Stress is a function of stacking fault energy and shear modulus. In [34] a model estimating the critical values of the stress and grain size, at which the emission of partial dislocations from grain boundaries and the start of the twinning process in nanostructured materials are possible, is proposed. The model's drawbacks are supposed to be immobility of a first partial dislocation in the process of emission of a second partial dislocation, miscalculation of the system energy, and the artificially introduced grain size. In [35] a correct three-dimensional model of emission of half-loops of split slip dislocations by grain boundaries in NS Al is proposed. The model accounts for the real geometry of dislocation slip and is based on precise calculation of the energy of elastically interacting dislocation loops. An anomalous width of stacking faults in NS Al is conditioned by the activity of external stress. At the same time, similarly to the approach suggested in [34], the anomalous width of stacking faults is also a grain size function (with the external stress absent). As follows from the model presented in [35], generally the width of stacking faults reduces when the grain size decreases. This result opposed the conclusions made in [34], which are a consequence of the artificially introduced grain size.

The conducted analysis demonstrates certain success in the description and analysis of the deformation behavior mechanisms of UFG and nanostructured metallic materials. At the same time, the mentioned models possess a number of weak points. For example, a cell structure is considered without concretizing the boundary structure and cell interiors in the models described in [21,24,25,28]. Unique properties of materials under SPD are a result of high volume fraction of grain boundaries, which play an important role during deformation of such materials. Specific properties of the structure and processes occurring during deformation keep in the background. This complicates studying the role of these or those deformation mechanisms. The misorientation evolution between neighboring cells is not considered. In the present paper an attempt has been made to develop a dislocation model, that could help to carry out a thorough analysis of the microstructure and deformation behavior evolution of pure metals (on the example of Cu) subjected to SPD.

2. BACKGROUND FOR THE UPGRADED DISLOCATION MODEL DEVELOPMENT

The development of the strain hardening models should be based on modern ideas about the character of microstructure evolution and mechanisms of SPD realization.

According to the experimental data, the collective behavior of dislocations complies with general rules when the strain degree increases [1]. Chaotic distribution of dislocations in a polycrystal at

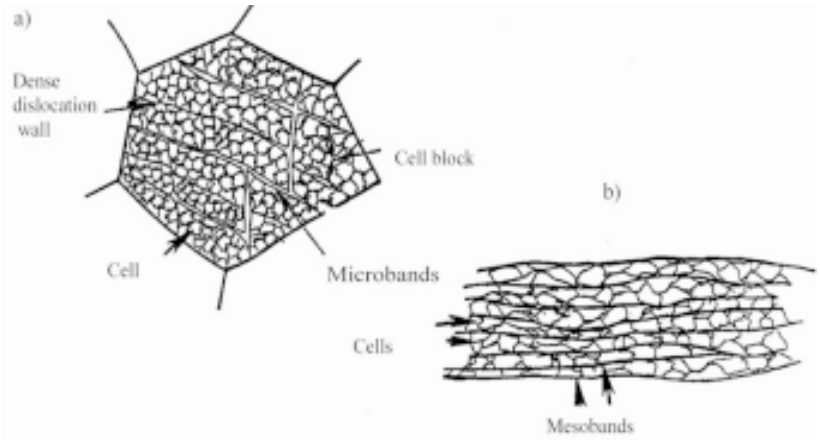

Fig. 1. Scheme of the deformation microstructure à) during small and mean strains by von Mises (e_{vm}=0.06-0.80); b) during large strains ($e_{vm}\geq 1$) [36].

the initial stages of deformation in a polycrystal becomes energetically unfavourable. As a result, a cell structure and then a fragmented one form. The latter one is characterized by high misorientation angles of fragments. Meanwhile, a cell structure sort "freezes" during plastic deformation. Fragmentation occurs on the background of the "frozen" cell structure. Only refinement of fragments takes place during further deformation and their relative half-turns increase (Fig. 1).

Processing of UFG and NS materials by the SPD technique is realized by incessant fragmentation of grains [3,36]; a specimen becomes highly fragmented. The fragment sizes remain practically unchanged in the process of the following plastic deformation [1]; perfection of interfragmentary boundaries takes place and misorientations between fragments increase. Mainly equi-axed microstructure forms with high-angle non-equilibrium grain boundaries as a result of SPD.

3. MAIN PROVISIONS OF THE ESTRIN – TÓTH MODEL

We shall first consider main provisions of the model [28] worked out by Estrin and Tóth to understand the details of the upgrading process. The conventional Estrin-Tóth model considers a composite structure of a cubic shape with a number of dislocations which form a cell structure as its structural element (Fig. 2). The neighboring cubic cells with the edge length *d* are separated by the walls with the thickness *w*, the volume fraction of which is

$$f = \frac{d^3 - (d-w)^3}{d^3}. \qquad (1)$$

It is assumed that the cell walls have also a cell structure. Then the Frank-Read sources, which are located on the wall surface, emit dislocations with the length *d-w* into the cell interiors. This leads to increase in the dislocation density in a cell body with the rate:

$$(\dot{\rho}_c)^+ = \frac{\alpha^*}{\sqrt{3}} \frac{\sqrt{\rho_w}}{b} \dot{\gamma}_w^r, \qquad (2)$$

where α^* is the coefficient of the effectiveness of the Frank-Read sources. The dislocation slip rate in the cell walls ν_w is expressed in terms of the resolved shear rate $\dot{\gamma}_w^r$ according to Orowan's formula: $\dot{\gamma}_w^r = \rho_w b \nu_w$, *b* - the value of the Burgers vector.

The dislocations leaving the cell interiors are integrated with the cell wall structure. Accounting for this process, the dislocation density in the cell body decreases with the rate

$$(\dot{\rho}_c)_w^- = -\beta^* \frac{6\dot{\gamma}_c^r}{bd(1-f)^{1/3}}, \qquad (3)$$

where β^* - the coefficient of the effectiveness of sink of dislocations in the cell walls. When deriving the formula (3), Orowan's ratio between the dislocation slip rate in the cell body ν_c and resolved strain rate $\dot{\gamma}_c^r$ was used: $\dot{\gamma}_c^r = \rho_c b \nu_c$.

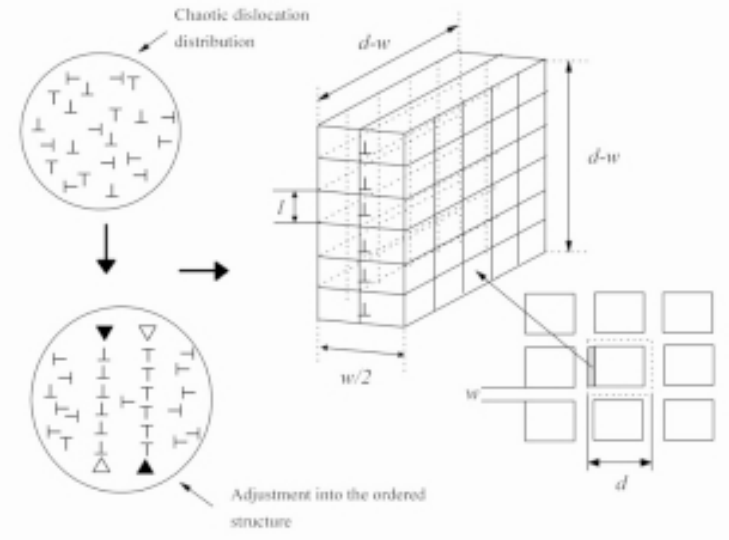

Fig. 2. An element of the fragmented structure.

With account of mutual annihilation of dislocations of opposite signs by a cross slip, the dislocation density in the cell body reduces according to the law:

$$\left(\dot{\rho}_c\right)^{-}_{cs} = -k_0\left(\frac{\dot{\gamma}^r_c}{\dot{\gamma}_0}\right)^{-1/n}\dot{\gamma}^r_c\rho_c. \tag{4}$$

The parameter k_0 characterizes the intensity of annihilation processes at T=0K, and n characterizes their sensitivity to strain rate during cross slip. With the stacking fault energy rising, the value of n grows and is inversely proportional to T, as the sensitivity of flow stress to the strain rate m [21].

As a result of the mentioned processes, the dislocation density inside the cells changes according to

$$\dot{\rho}_c = \alpha * \frac{1}{\sqrt{3}}\frac{\sqrt{\rho_w}}{b}\dot{\gamma}^r_w - \beta * \frac{6\dot{\gamma}^r_c}{bd\left(1-f\right)^{1/3}} - k_0\left(\frac{\dot{\gamma}^r_c}{\dot{\gamma}_0}\right)^{-1/n}\dot{\gamma}^r_c\rho_c. \tag{5}$$

The dislocations leaving the cell interiors are integrated into the cell wall structure causing growth of the dislocation density in the walls with the rate

$$\left(\dot{\rho}_w\right)^{+} = \frac{6\beta * \dot{\gamma}^r_c\left(1-f\right)^{2/3}}{bdf}. \tag{6}$$

The increase in the dislocation density results in reduction of the length of dislocation segments in the boundaries and increase of shearing stresses necessary for the activity of Frank-Read sources. The growth of the applied stress allows keeping the activity of the existing sources and also leads to activation of new ones. As a result the dislocation density will grow with the rate

$$\left(\dot{\rho}_w\right)^{+(FR)} = \frac{\sqrt{3}\beta * \dot{\gamma}^r_c\left(1-f\right)\sqrt{\rho_w}}{fb}. \tag{7}$$

Due to the annihilation of dislocations at the expense of cross slip in the cell walls, the dislocation density decreases with the rate

$$\left(\dot{\rho}_w\right)^{-}_{cs} = -k_0\left(\frac{\dot{\gamma}^r_w}{\dot{\gamma}_0}\right)^{-1/n}\dot{\gamma}^r_w\rho_w. \tag{8}$$

The total contribution of all the considered processes can be stated by the equation:

$$\dot{\rho}_w = \frac{6\beta * \dot{\gamma}^r_c\left(1-f\right)^{2/3}}{bdf} + \frac{\sqrt{3}\beta * \dot{\gamma}^r_c\left(1-f\right)\sqrt{\rho_w}}{fb} - k_0\left(\frac{\dot{\gamma}^r_w}{\dot{\gamma}_0}\right)^{-1/n}\dot{\gamma}^r_w\rho_w. \tag{9}$$

It is considered that the cell size is proportional to the dislocation density

$$d = \frac{K}{\sqrt{\rho_{total}}}, \quad (10)$$

where K – the proportionality constant, ρ_{total} - the total dislocation density, which is calculated as

$$\rho_{total} = f\rho_w + (1-f)\rho_c. \quad (11)$$

Eq. (10) cannot be interpreted as a homothety with the coefficient K. In other words, defining the wall thickness w as an image of $1/\sqrt{\rho_{total}}$

$$w = \frac{K'}{\sqrt{\rho_{total}}} \quad (12)$$

we get w/d=const and, therefore, the volume fraction of cell walls f is also constant. Such a statement does not agree with the experimental data. As a result of data integration, the resolved strain dependence of the volume fraction of cell walls f was derived in [20] as:

$$f = f_\infty + (f_0 - f_\infty)\exp\left(-\gamma^r / \tilde{\gamma}^r\right), \quad (13)$$

where f_0, f_∞ - its initial and limited values, $\tilde{\gamma}^r$ - the parameter characterizing the rate of decrease of f depending on the resolved strain γ^r.

The resolved stresses τ_w^r and τ_c^r in the cell walls and interiors are calculated with account of the corresponding dislocation densities ρ_w and ρ_c

$$\tau_w^r = \alpha G b\sqrt{\rho_w}\left(\frac{\dot{\gamma}_w^r}{\dot{\gamma}_0}\right)^{1/m}, \quad (14)$$

$$\tau_c^r = \alpha G b\sqrt{\rho_c}\left(\frac{\dot{\gamma}_c^r}{\dot{\gamma}_0}\right)^{1/m}, \quad (15)$$

where G is the shear modulus, b – the Burgers vector, $\dot{\gamma}_0$ - the pre-exponential factor, $1/m$ – the value opposite to the sensitivity of flow stress to strain rate, α - the constant that reflects interactions between dislocations.

The deformation behavior of the composite is defined by the resolved stress τ^r connected with the resolved stresses τ_w^r and τ_c^r according to the rule

$$\tau^r = f\tau_w^r + (1-f)\tau_c^r. \quad (16)$$

To fulfill the conditions of strain compatibility along the phase division boundary (the cell interiors and walls), it is considered that $\dot{\gamma}_w^r = \dot{\gamma}_c^r = \dot{\gamma}^r$.

The model parameters α^*, β^*, K, k_0 are defined by approximating the modeling flow curve to the experimental points. The 3D model is used in combination with the VPSC model of polycrystals. This helps tracing the dependence of hardening curves on the deformation modes and texture evolution [29].

At the same time, the Estrin-Tóth model considers a cell structure of cubic shape without specifying the structure of cell interiors or boundaries. The authors do not account for the peculiarities of structure and processes which take place during deformation of UFG and NS materials mentioned above. In particular, the evolution of misorientations between neighboring cells and grains is not taken into account. The nature of other sources and sinks of defects in the cell boundaries and interiors, except Frank-Read sources, and annihilation of screw dislocations during double cross slip is not specified. The boundary structure and its influence on the formation of special mechanical properties of UFG and NS materials constitute a major problem in physics of such materials [37] (Fig. 1a), but they are not considered in this model.

The model does not enable calculating misorientations between cells, as it does not consider the density of excess dislocations in the cell walls. As a result, it may be successfully used for simulation of large plastic strains for which low-angle misorientations are typical (Fig. 1b), but the model requires upgrading in the case of SPD materials, since they have a UFG structure with mainly high-angle misorientations between grains. The aim of this paper is to upgrade the Estrin-Tóth dislocation model for adequate accounting of peculiarities of structure evolution and deformation behavior of SPD metals with fcc lattice.

4. MAIN PROVISIONS OF THE UPGRADED MODEL

According the experimental data [1,4], we shall consider that the structure of an SPD material consists of cell blocks/fragments which are separated by the boundaries containing excess dislocations ‘fluffed’ by non-excess sessile dislocations [3] (Fig. 2). We shall designate such a structure as a fragmented one with the fragment size d. Dislocations in the fragment interior form a cell structure with the total density of immobilized dislocations in the cell walls and their interiors equaling to ρ_c. Accounting of the total dislocation density ρ_w and the density of non-excess sessile dislocations ρ_f in the fragment boundaries will enable calculating the den-

sity of excess dislocations in the boundaries and misorientations between the fragments. The volume fraction of fragment boundaries is calculated according to formula (1).

Annihilation of dislocations during their non-conservative movement conditioned by vacancy diffusion and annihilation of edge dislocations are considered to explain the absence of hardening on the stage of severe plastic strain. Material flow is considered to be supported by dislocation generation during multiple cross slip [38].

4.1. Evolution of the dislocation density in the fragment boundaries

Basing on the experimental data, we shall give mathematical description of physical processes which govern the evolution of the dislocation density in the fragment boundaries. As in case of the conventional Estrin-Tóth model, an increase in the dislocation density in the fragment boundaries is considered to occur at the expense of the dislocations coming from the interiors (6) and the activity of the Frank-Read sources (7). It is supposed that emission of the stored deformation energy is carried out by annihilation of screw dislocations as a result of double cross slip, typical for the beginning of stage III of the strain hardening [15]

$$\dot{\rho}_w^- = -\frac{\delta_\alpha \dot{\gamma}^r \rho_w}{b}, \tag{17}$$

where δ_α - the coefficient of annihilation of screw dislocations. In [39,40] the following expression was derived

$$\frac{\delta_\alpha}{b} = \chi_\alpha = \chi_\alpha(0) e^{\frac{k_b T}{A} \ln\left(\frac{\dot{\gamma}_0}{\dot{\gamma}^r}\right)}, \tag{18}$$

where $\chi_\alpha(0)$ is the annihilation coefficient at T=0K, k_b - the Boltzman constant, A – the constant depending on the stacking fault energy.

The stacking fault energy W of Cu is 0.050 J/m^2, see [41]. According to the dependence of $A/(G*b^3)$ on $W/(G*b)$ [40], the exponent is defined as $n=A/k_bT$. n=37 for Cu at homologous temperature T/T_m=0.2 which corresponds to room temperature.

The defect structure and specific deformation mechanisms of nanomaterials influence the dynamics of the dislocation density. This fact suggests that the fragment boundaries include non-excess sessile and excess edge dislocations with the Burgers vector perpendicular to the boundary. The increase in the dislocation density of fragment boundaries leads to the increase of misorientations between fragments [4].

Mobile dislocations can annihilate with non-excess sessile dislocations, the density of which is indicated as ρ_f. The annihilation of edge dislocations is discussed in [42], where it is shown that the edge dislocations of opposite signs annihilate at distances smaller than the annihilation length which equals to 1.6 nm. As a result, the dislocation density decreases in the boundaries with the rate:

$$\dot{\rho}_w^- = -R_f \rho_f \dot{\gamma}^r / b. \tag{19}$$

where R_f is the annihilation length.

The dislocation density in the fragment boundaries reduces as a result of the annihilation of non-excess sessile edge dislocations, which is conditioned by their non-conservative motion due to vacancy capture [43]. Climb of dislocations may occur only on condition that the diffusional mass transfer between a dislocation and a surrounding medium is possible. The diffusional flux on a dislocation occurs due to oversaturation of point defects in the considered volume. Such a flux is also caused by the force acting on a dislocation in the direction normal to its slip plane.

According to [44], the dislocation density decreases as a result of the vacancy diffusion through the tube surrounding the dislocation core according to

$$\frac{d\rho_w^-}{dt} = -\phi' \rho_f^3, \tag{20}$$

where ϕ' - the function of vacancy concentration. The hypothesis is that the increment coefficient of the dislocation density ρ_f is $1/\tau$. Then the decrease rate of the density of non-excess sessile dislocations during their non-conservative motion is

$$\frac{d\rho_w^-}{dt} = -\frac{\rho_f}{\tau}, \tag{21}$$

where τ - the annihilation time.

Parallel edge dislocations in different but parallel slip planes achieve one another only by way of climbing, which is possible only during the diffusional mass transfer. Let axis 0x is directed along the Burgers vector (Fig. 3). A pair of dislocations climbing towards each other with the rate υ_c under the activity of the corresponding component σ_{xx} of the stress deviator tensor in a sample which is affected by uniaxial tensile stress σ from starting positions, corresponding to the stable configura-

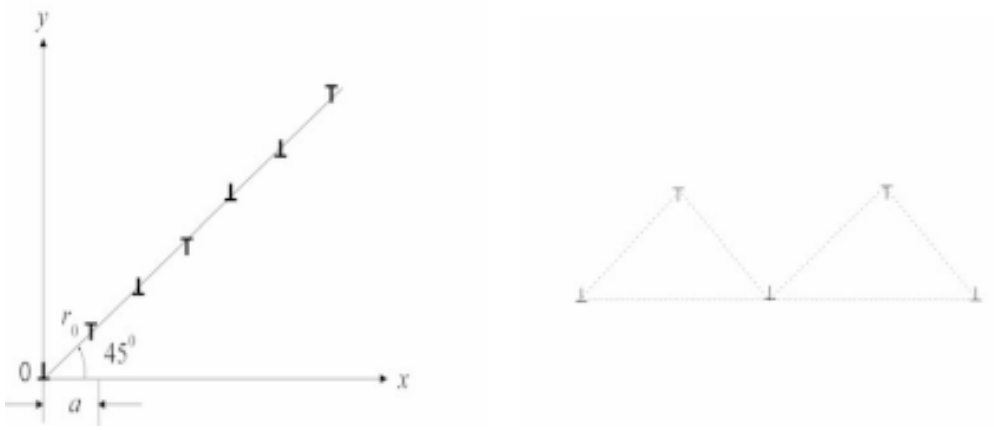

Fig. 3. Stable configuration of dislocations of opposite signs.

tion (Fig. 3) [41], annihilates in the time τ which needs to be estimated. The rate of the relative dislocation motion is $2\nu_c$ here.

If the dislocations are separated by $a = r\cos 45^\circ = r\sqrt{2}/2$, then $da/d\tau = 2\nu_c$, $d\tau = da/2\nu_c$, where r is the running value of the distance between the dislocations. Integrating the last equation, we receive

$$\tau = \frac{1}{2\sqrt{2}} \int_0^{r_0} \frac{dr}{\nu_c}, \tag{22}$$

where r_0 is the initial distance between the dislocations.

The flux of vacancies emerges in a sample, if the energy of vacancy formation at the expense of the applied external tensile stress along x axis is different in different points of a sample. This mass-transfer results in the plastic deformation, the rate of which depends on the rate of dislocation climbing υ_c. σ_{xx} - the corresponding stress deviator tensor component, arising as a result of interaction of the dislocation pair, is the reason of the climb of dislocations with the rate $\upsilon_c = B'/2\sqrt{2}\,r r_0^2$. Then, after integrating Eq. (22), we get

$$\tau = \frac{r_0^4}{2B'}. \tag{23}$$

Taking into account $\rho_f = 1/r_0^2$, we receive the following

$$\frac{d\rho_f}{dt} = -2B'\rho_f^3, \tag{24}$$

where

$$B' = \sqrt{2}\,/\left[\pi(1-\nu)\right] D_c q_c (G\Omega / kT),$$
$$D_c = D_{c0} C_\nu \exp\left(-H_c^m / kT\right). \tag{25}$$

C_ν - the concentration of vacancies which form during deformation, H_c^m - the enthalpy of the activation of the vacancy migration along the dislocation nuclei which is equal to 0.2 eV according to [24], Ω - the atomic volume in Cu, $\Omega = 1.1\cdot 10^{-29}\,m^3$, q_c - the square of the cross section of the dislocation core, $q_c = b^2$, G – the shear modulus, D_c - the diffusion coefficient along the dislocation core, the multiplier D_{c0} is accepted in accordance with [24], $D_{c0}=10^{-4}$ m^2/s, ν - the Poisson ratio, ν =0.343 [27].

Using Eq. (20), the function $\phi = \phi'/\dot{\gamma}^r$ against $d\rho_w/dt$ is constructed by going over from t to γ^r , ϕ is proportional to the vacancy concentration C_v here. At the first approximation, we consider that the vacancy concentration (the function ϕ) depends linearly on the deformation γ^r with the proportionality constant C, that's why we can write

$$\phi\left(\left.\frac{d\rho_w}{d\gamma^r}\right|_{t+1}\right) = \phi\left(\left.\frac{d\rho_w}{d\gamma^r}\right|_{t}\right) + \left.\frac{d\rho_w}{d\gamma^r}\right|_{t} C d\gamma^r. \tag{26}$$

The density of non-excess sessile dislocations ρ_f, which is part of the dislocation density in the fragment boundaries ρ_w, changes according to the law (20). Comparing the corresponding annihilation constituent in Eq. (24) with expression (20) , we receive $\phi' = 2BC_\nu$, where $B = B'/C_\nu$. In the non-dimensional view, after introducing non-dimen-

sional magnitudes $\widetilde{B}$, $\widetilde{\dot{\gamma}}^r$, and $\widetilde{\phi}'$, $B\rho_{0w}^2 t_0 \to \widetilde{B}$, $\phi\rho_{0w}^2 t_0 \to \widetilde{\phi}$, $\dot{\gamma}^r t_0 \to \widetilde{\dot{\gamma}}^r$, $\widetilde{\phi}' = \widetilde{\phi}\widetilde{\dot{\gamma}}^r$, where $t_0 = 1/\dot{\gamma}_0$, the last equation is $\widetilde{\phi}' = 2\widetilde{B}C_v$. Depending on deformation, the vacancy concentration is $C_v = \widetilde{\phi}' / 2\widetilde{B}$.

While including noncomplanar slip systems during deformation, dislocation generation on the "forest" dislocations crossing the given slip plane becomes predominant [38]:

$$\dot{\rho}_w = \frac{\delta_f \rho_f^{1/2} \dot{\gamma}^r}{b}, \tag{27}$$

where δ_f is the coefficient of dislocation generation on the "forest" dislocations, the density of which is ρ_w. It is stated in [38] that $\delta_f \approx 10^{-2}$ at high dislocation densities. The dislocation densities in the primary and secondary slip systems are comparable at the beginning of stage II of the strain hardening and increase with the deformation. That results in the annihilation of screw components of dislocation loops at low and moderate temperatures. Due to this, stage III emerges on the flow curve [45].

The length of dislocations moving from the interiors to the fragment boundaries is $\beta^*\rho_c \nu_c dt(d-w)^2$ [28]. The fraction of immobilized dislocations is designated as P_f. Then it can be expected that the dislocation density will grow as

$$\dot{\rho}_f^+ = \frac{6P_f \beta^* \dot{\gamma}^r (1-f)^{2/3}}{bdf}. \tag{28}$$

Thus, summing up Eqs. (7), (17), (19), (24), (27), and (28), the evolution of the total dislocation density can be described with the help of the expression:

$$\dot{\rho}_w = \frac{6P_f \beta^* \dot{\gamma}^r (1-f)^{2/3}}{bdf} + \frac{\sqrt{3}\beta^* \dot{\gamma}^r (1-f)\sqrt{\rho_w}}{fb} + \frac{\delta_f \rho_f^{1/2} \dot{\gamma}^r}{b} - \frac{\delta_\alpha \rho_w \dot{\gamma}^r}{b} - \frac{R_f \rho_f \dot{\gamma}^r}{b} - 2B'\rho_f^3. \tag{29}$$

The density of non-excess sessile dislocations changes with time as follows

$$\dot{\rho}_f = \left(\frac{6P_f \beta^* \dot{\gamma}^r (1-f)^{2/3}}{bdf} + \frac{\sqrt{3}\beta^* \dot{\gamma}^r (1-f)\sqrt{\rho_w}}{fb} + \frac{\delta_f \rho_f^{1/2} \dot{\gamma}^r}{b} \right) P_f' - \frac{R_f \rho_f \dot{\gamma}^r}{b} - 2BC_v \rho_f^3, \tag{30}$$

where P_f' is the fraction of the "forest" dislocations among all the dislocations, which came into the fragment boundaries.

4.2. Evolution of dislocation density in the fragment interiors

An increase in the dislocation density in the fragment interiors is considered to take place on account of influence of the Frank-Read sources (2). The reduction of the dislocation density is conditioned by annihilation during cross slip (4) and sink of dislocations from interiors into the fragment boundaries (3). Describing the evolution of the dislocation density in the fragment interiors, one should note that the dislocation generation should be additionally taken into account after multiple cross slip [38].

$$\dot{\rho}_c = \frac{\delta_f \rho_c^{1/2} \dot{\gamma}^r}{b}. \tag{31}$$

Taking into account the contribution of all the above-mentioned processes, we can state that the dislocation density inside the fragment changes according to

$$\dot{\rho}_c = \alpha^* \frac{1}{\sqrt{3}} \frac{\sqrt{\rho_w}}{b} \dot{\gamma}^r + \frac{\delta_f \rho_c^{1/2} \dot{\gamma}^r}{b} - \beta^* \frac{6\dot{\gamma}^r}{bd(1-f)^{1/3}} - \chi_0 \dot{\gamma}^r \rho_c. \tag{32}$$

4.3. Formalism of the upgraded model

It is supposed that within the upgraded model the resolved shear stress is calculated according to formulas (14), (15), (16). Introducing non-dimensional variables:

$$\frac{\rho_w}{\rho_{0w}} \to \widetilde{\rho}_w, \frac{t}{t_0} \to \widetilde{t}, \frac{\rho_f}{\rho_{0w}} \to \widetilde{\rho}_f, \frac{\rho_c}{\rho_{0c}} \to \widetilde{\rho}_c,$$
$$b\sqrt{\rho_{0w}} \to \widetilde{b},$$
$$d\sqrt{\rho_{0w}} \to \widetilde{d}, \frac{G}{\tau_0^r} \to \widetilde{G}, \frac{\tau_w^r}{\tau_0^r} \to \widetilde{\tau}_w^r, \frac{\tau_c^r}{\tau_0^r} \to \widetilde{\tau}_c^r, \tag{33}$$
$$\frac{\dot{\gamma}^r}{\dot{\gamma}_0} = \dot{\gamma}^r t_0 \to \widetilde{\dot{\gamma}}^r, \frac{R_f}{b} \to \widetilde{R}_f,$$

where τ_0^r - the yield stress.

Bringing together Eqs. (14), (15), (28), (29), and (32), the obtained system of equations can be written in the dimensionless form:

$$\begin{cases} \dfrac{d\tilde{\rho}_w}{d\tilde{t}} = \dfrac{6P_f\beta^*\dot{\tilde{\gamma}}^r(1-f)^{2/3}}{\tilde{b}\tilde{d}f} + \dfrac{\sqrt{3}\beta^*\dot{\tilde{\gamma}}^r(1-f)\sqrt{\tilde{\rho}_w}}{f\tilde{b}} + \\ \dfrac{\delta_f\tilde{\rho}_f^{1/2}\dot{\tilde{\gamma}}^r}{\tilde{b}} - \chi_a\dot{\tilde{\gamma}}^r\tilde{\rho}_w - \tilde{R}_f\tilde{\rho}_f\dot{\tilde{\gamma}}^r - \tilde{\phi}\tilde{\rho}_f^3 \\ \dfrac{d\tilde{\rho}_f}{dt} = \left(\dfrac{6P_f\beta^*\dot{\tilde{\gamma}}^r(1-f)^{2/3}}{\tilde{b}\tilde{d}f} + \dfrac{\sqrt{3}\beta^*\dot{\tilde{\gamma}}^r(1-f)\sqrt{\tilde{\rho}_w}}{f\tilde{b}} + \right. \\ \left. \dfrac{\delta_f\tilde{\rho}_f^{1/2}\dot{\tilde{\gamma}}^r}{\tilde{b}} \right) P_f' - \tilde{R}_f\tilde{\rho}_f\dot{\tilde{\gamma}}^r - \tilde{\phi}\tilde{\rho}_f^3 \\ \dfrac{d\tilde{\rho}_c}{d\tilde{t}} = \dfrac{\alpha^*\sqrt{\tilde{\rho}_w}\dot{\tilde{\gamma}}^r}{\sqrt{3}\tilde{b}} + \dfrac{\delta_f\sqrt{\tilde{\rho}_c}\dot{\tilde{\gamma}}^r}{\tilde{b}} - \\ \dfrac{6\beta^*\dot{\tilde{\gamma}}^r}{\tilde{b}\tilde{d}(1-f)^{1/3}} - \chi_a\tilde{\rho}_c\dot{\tilde{\gamma}}^r \\ \tilde{\tau}_w^r = \alpha\tilde{G}\tilde{b}\sqrt{\tilde{\rho}_w}\left(\dot{\tilde{\gamma}}^r\right)^{1/m},\ \tilde{\tau}_c^r = \alpha\tilde{G}\tilde{b}\sqrt{\tilde{\rho}_c}\left(\dot{\tilde{\gamma}}^r\right)^{1/m} \end{cases} \quad (34)$$

The total dislocation density, the fragment size (in non-dimensional variables), and the evolution of the volume fraction of fragment boundaries are calculated here using expressions (11), (10), (13).

4.4. Calculation of misorientations between neighboring fragments

One of the upgrading points for the Estrin-Tóth dislocation model was the consideration of the misorientation angle between the neighboring fragments. The excess dislocation density in the boundaries can be defined as the difference between the total dislocation density ρ_w and the density of non-excess sessile dislocations ρ_f in the fragment boundaries:

$$\rho_{exc} = \rho_w - \delta_f. \quad (35)$$

Basing on the calculated excess dislocation density, the distance between the neighboring dislocations in the cell walls h is

$$h = \frac{1}{d\rho_{exc}}. \quad (36)$$

Misorientations between the neighboring cells were calculated according to the approach proposed in [46]:

$$\theta = \frac{b}{h} = bd\rho_{exc}. \quad (37)$$

4.5. Account of the evolution of crystallographic texture

To consider the influence of the crystallographic texture, the values of the reduced rates $\dot{\gamma}_s^r$ in each slip system of a grain (fragment) were obtained with the help of the VPSC model. The shear rate in a grain at rather high rate sensitivities was taken equaling

$$\dot{\gamma}^r \approx \sum_{s=1}^{k} \dot{\gamma}_s^r, \quad (38)$$

where k is the number of active slip systems. The correctness of the last equation is shown in [28].

A polycrystal was presented as the values of weighted orientations. Orientations were connected with grains and their weights were defined by volume fractions. Crystallographic texture of a sample was described with the help of these values.

Every grain is a viscoplastic ellipsoid placed in the effective viscoplastic medium averaged in all the grains. Deformation is carried out by slipping in all slip systems activated by the resolved shear stresses. It is considered that the dependence of the resolved strain rate tensor $\dot{\gamma}^r$ on the stress tensor σ^c is correct for any separate grain

$$\dot{\gamma}_{ij}^r = \dot{\gamma}_0 \sum_s \frac{g_{ij}^s g_{kl}^s}{\tau^s} \left(\frac{g^s : \sigma}{\tau^s} \right)^{m-1} \sigma_{kl} = M_{ijkl}^c \sigma_{kl}^c, \quad (39)$$

where s is a number of the slip system, g^s - Schmid's tensor, τ^s - the threshold shear stress, and σ – the applied external stress.

The equation of interaction between the inclusion and effective medium, on which the self-consistent model is based, was used in the form

$$\left(\dot{\gamma}^r - \bar{\dot{\gamma}}^r\right) = n^{eff}\left(1-E\right)^{-1} : E : \overline{M}^{sec}\left(\sigma^c - \bar{\sigma}\right), \quad (40)$$

where $\bar{\dot{\gamma}}^r$, $\bar{\sigma}$ are the overall rate of the resolved strain and overall stress, respectively, E – Eshelby's tensor, which is a homogeneous function of the overall compliance and the ratio of ellipsoid axes, $\overline{M}^{sec}$ - overall secant viscoplastic compliance depending on the stress in a sample. The parameter n^{eff} makes it possible to receive the Taylor approximation ($n^{eff} = 0$), tangent ($n^{eff} = m$), and secant ($n^{eff} = 1$) approximations, Sach's approximation ($n^{eff} = \infty$). The case at which $1 < n^{eff} < m$ considers the differ-

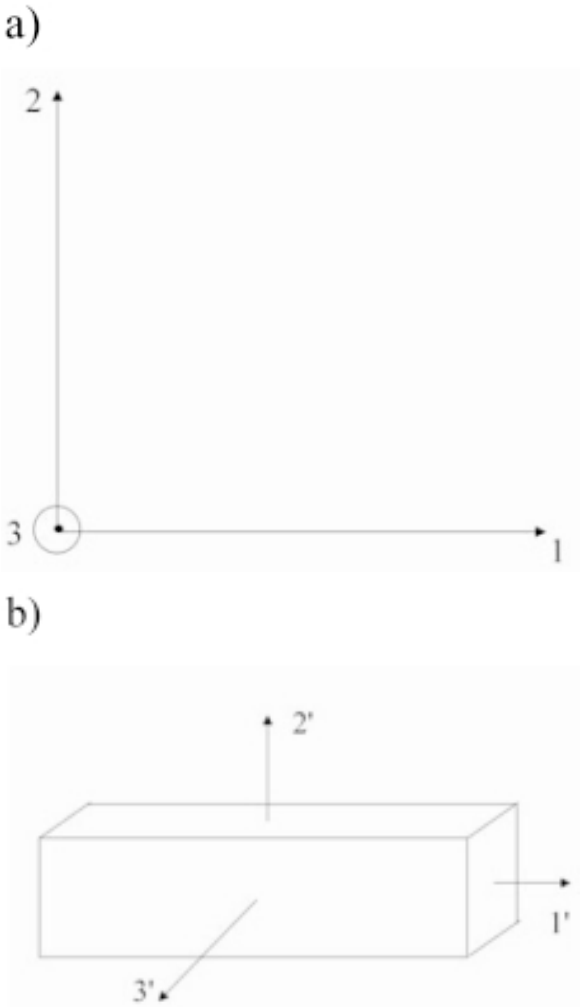

Fig. 4. 1, 2, 3 – axes of the global coordinate system (à), 1', 2', 3' - axes of the coordinate system, connected with the sample (b).

ence of interaction between each separate grain and effective medium [47]. In the present paper m is taken equal to 185, that is 5 times larger than the exponent n in Eq. (17) (i.e. $n >> 1$, but $m > n$) and tangential approximation corresponds to the Estrin-Tóth model.

The Taylor factor M was defined as the ratio of the average sum of the resolved strain rates $\dot{\gamma}_s^r$ in all the slip systems to the given strain rate $\dot{\varepsilon}$ [21]:

$$M = \frac{\sum_{i=1}^{N}\left(\sum_{s=1}^{L}\dot{\gamma}_s^r\right)V_i}{\dot{\varepsilon}}, \qquad (41)$$

where V_i is the volume fraction of grains with the given orientation, N - the number of grains, L – the number of slip systems. The generalized Taylor factor which corresponds to tension of a polycrystal material was calculated as

$$M^*_{tention} = \frac{\bar{\dot{\gamma}}^r}{\dot{\varepsilon}}, \qquad (42)$$

where $\dot{\varepsilon}$ is the macroscopic strain rate. At that, the following formula was taken into account

$$\bar{\gamma}^r = \int_0^t \left(\sum_{i=1}^{N}\left(V_i\dot{\gamma}_i^r\right)\right)dt. \qquad (43)$$

5. PROCEDURE OF SIMULATION AND EXPERIMENTS

ECAP is a cyclic process which consists in multiple pushings of a sample through the two channels with equal sections intersecting at an angle $90^o \le \phi \le 157.5^o$ [47,48] along different routes. When modeling a regular ECAP pass, the data obtained during the previous deformation stage were used as input parameters. The route B_c, considered in this paper, is performed by turning the morphologic and crystallographic textures clockwise about axis 3 of the global coordinate system 1, 2, 3 (Fig. 4a). At that, axes 1', 2', 3' of the coordinate system which is connected with the sample coincide with the axes 2, 1, and 3 of the global coordinate system respectively (Fig. 4b). (When coming out of the die channel, axes 1', 2', 3' of the connected coordinate system coincide with axes 1, 2, 3 of the global coordinate system). The second rotation is carried out clockwise about axis 2 of the global coordinate system (axis 1' of the connected system) after each pass.

At each pass of ECAP along the route B_c, the specimen is subjected to simple shear along the plane that is oriented at an angle $\varphi = \phi/2$. The shear planes intersect at every following pass. The shear at the 3rd pass is reverse in respect to the shear at the 1st pass. The shear at the 4th pass is reverse to the shear at the 2nd pass. The pattern of the deformation path is repeated in every 4th pass.

When modeling tension of a sample, the data obtained at the end of simulation of the succeeding ECAP pass were used as input parameters. The Taylor factor was calculated at every deformation step with the help of the obtained volume fractions V_i and resolved rates $\dot{\gamma}_s^r$ in each slip system according to the Eq. (41).

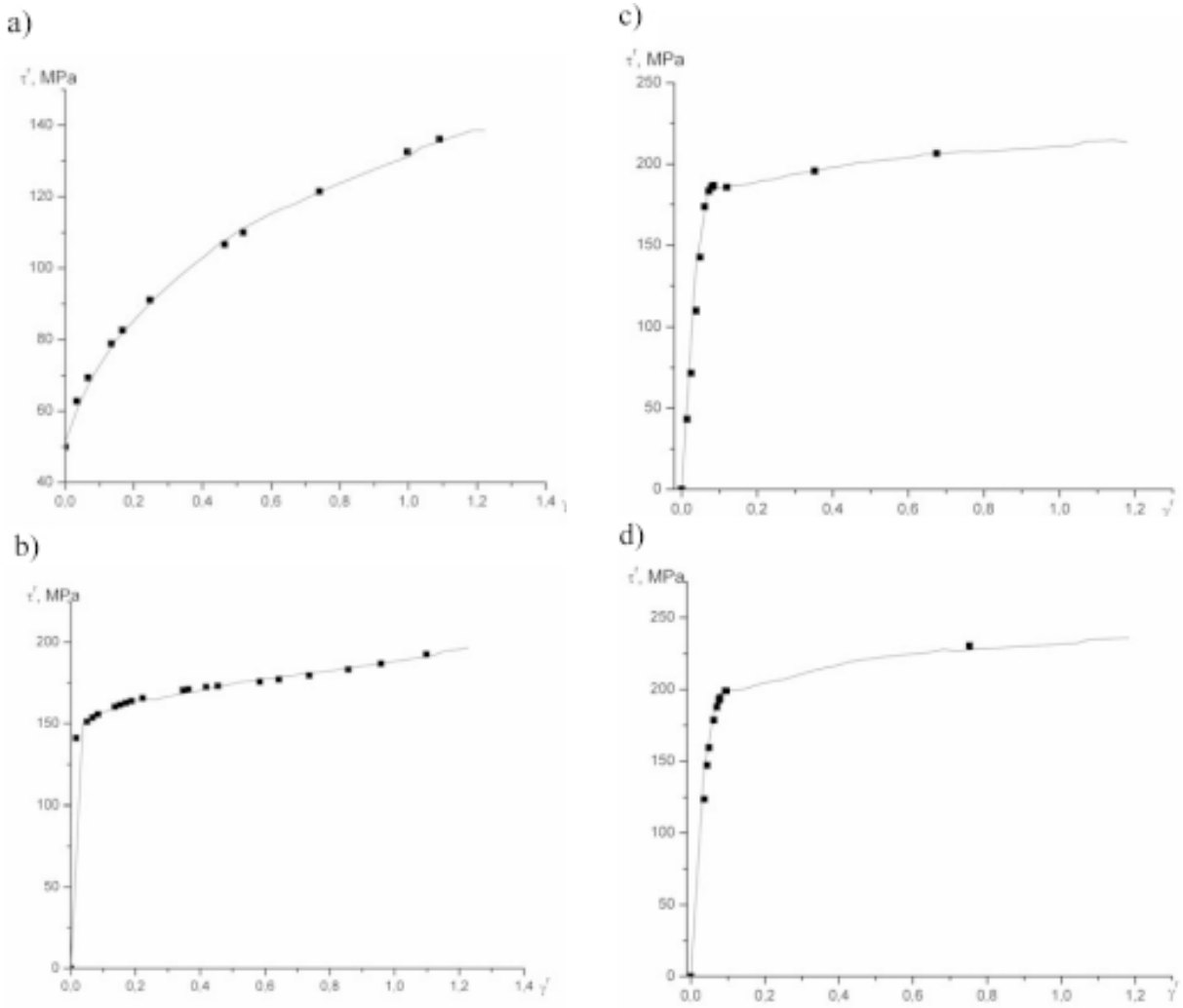

Fig. 5. Experimental (■) and modeling curves (-) of the flow stress dependence of the tension degree of Cu (evolution of the Taylor factor is taken into account): initial state (a), after 1(b), 4(c), and 8(d) passes of ECA-pressing along the route B_c.

The angle of channel's intersection during ECAP was 90°. The punch displacement velocity was 50 mm/min, the test was carried out at room temperature. The samples for ECAP had the size of 60×8×8 mm^3 .

Mechanical tensile tests of the pure Cu sample annealed at 550 °C during one hour (in the initial state) and Cu after the 1st, 4th, and 8th passes of ECAP along the route B_c were carried out on the universal dynamometer INSTRON 1185 at room temperature with the initial strain rate $5.5 \cdot 10^{-4}$ s^{-1}. The diameter of the working part of a sample for mechanical testing was 3 mm, and the length was 15 mm. True stress was defined as the ratio of the applied stress to the cross section of a sample calculated with the help of the condition of deformation uniformity and stability of the sample volume. The true strain was counted as $\varepsilon = \ln(F_0/F_T)$, where F_T is the current value of the cross section area and F_0 is the initial value of the cross section area. The samples were subjected to grinding and polishing.

The plastic flow of samples was heterogeneous along the sample length; this led to localization of plastic strain. Elongation to failure of the initial sample and the samples after the 1st, 4th, and 8th ECAP passes was 45%, 15%, 10% and 11%; the yield stress was 227 MPa, 376 MPa, 436 MPa, and

Table 1. Initial values of the dislocation densities in the samples taken in different structural states.

Parameters	As-received	1 pass route B_c	4 passes route B_c	8 passes route B_c
$\rho_w(\gamma^r = 0.0)$, m^{-2}	$5.0*10^{14}$	$4.9*10^{15}$	$1.4*10^{16}$	$1.8*10^{16}$
$\rho_c(\gamma^r = 0.0)$, m^{-2}	$2.5*10^{14}$	$5.7*10^{14}$	$6.5*10^{14}$	$9.0*10^{14}$

Table 2. The values of the parameters used for modeling.

Parameters	Values	Parameters	Values
f_∞	0.060	G, GPa	42.1
$\tilde{\gamma}^r$	3.2	m	185
$\dot{\gamma}_0$, s^{-1}	1	n	37
δ_f	0.013	b, nm	0.256

460 MPa, and the failure stress was 415 MPa, 600 MPa, 680 Mpa, and 740 MPa, respectively.

An algorithm and a software (Fortran 77) were developed with to perform calculations in accordance the above-mentioned equations. Calculations were carried out for the wide range of variable parameters, which were chosen regarding for the available experimental data and physical significance.

A polycrystalline sample was assumed to consist of 830 weighted orientations. It was supposed that up to 12 octahedral slip systems {111}<110> typical of fcc lattice could operate. The threshold shear stress was the same for all the slip systems. The parameters used during modeling of tension of Cu in the initial state and after the 1st, 4th, and 8th ECAP passes along the route B_c are presented in Tables 1 and 2. The values of the dislocation densities ρ_w and ρ_c were chosen according to the data from [49-51]. It has been taken into account that the modeling results are insensitive to the initial values of variables in the considered interval of deformation as stated in [30].

The parameters α^*, β^*, K', C, P_f, $\tilde{R}_f$, $\chi_a(0)$ were obtained approximating the modeling curves to the experimental points by the least-square method. The simulation was carried out with the true strain of 0.51, at which the section in the neck decreased almost 1.6 times. Accounting of texture, the calculation of the resolved stresses was carried out by the technique described in [28]. The constant of the dislocation interaction α was estimated from the values of the volume fraction f and resolved stress τ^r obtained via Eq. (16) using the values of the dislocation densities ρ_w and ρ_c taken from [28].

6. MODELING RESULTS AND DISCUSSION

Fig. 5 shows the experimental data obtained during tensile testing of Cu samples in the as-received state and after the 1st, 4th, and 8th passes of ECAP along the route B_c.

Stage III of the strain hardening is clearly observed on the flow curve of the initial state. The character of the flow curve after the 1st, 4th, and 8th ECAP passes is more complicated. Stages III and IV of the strain hardening are distinguishable. The modeling curves obtained for the given states correspond to the experimental data. The above-mentioned peculiarities of the deformation behavior of Cu are also observed on the modeling of hardening rate - resolved strain curves (Fig. 6). Stage III of the strain hardening for Cu subjected to ECAP is characterized by a much higher hardening rate as compared to stage III of hardening of the as-received Cu. This is due to much higher degree of the accumulated strain.

The experimental points were presented as the dependence “resolved stress - resolved strain” to be compared with the modeling curves (Fig. 5). Basing on this aim, the integral Taylor factor M^* was counted for a polycrystalline. The Taylor factor values corresponded to the tension of the

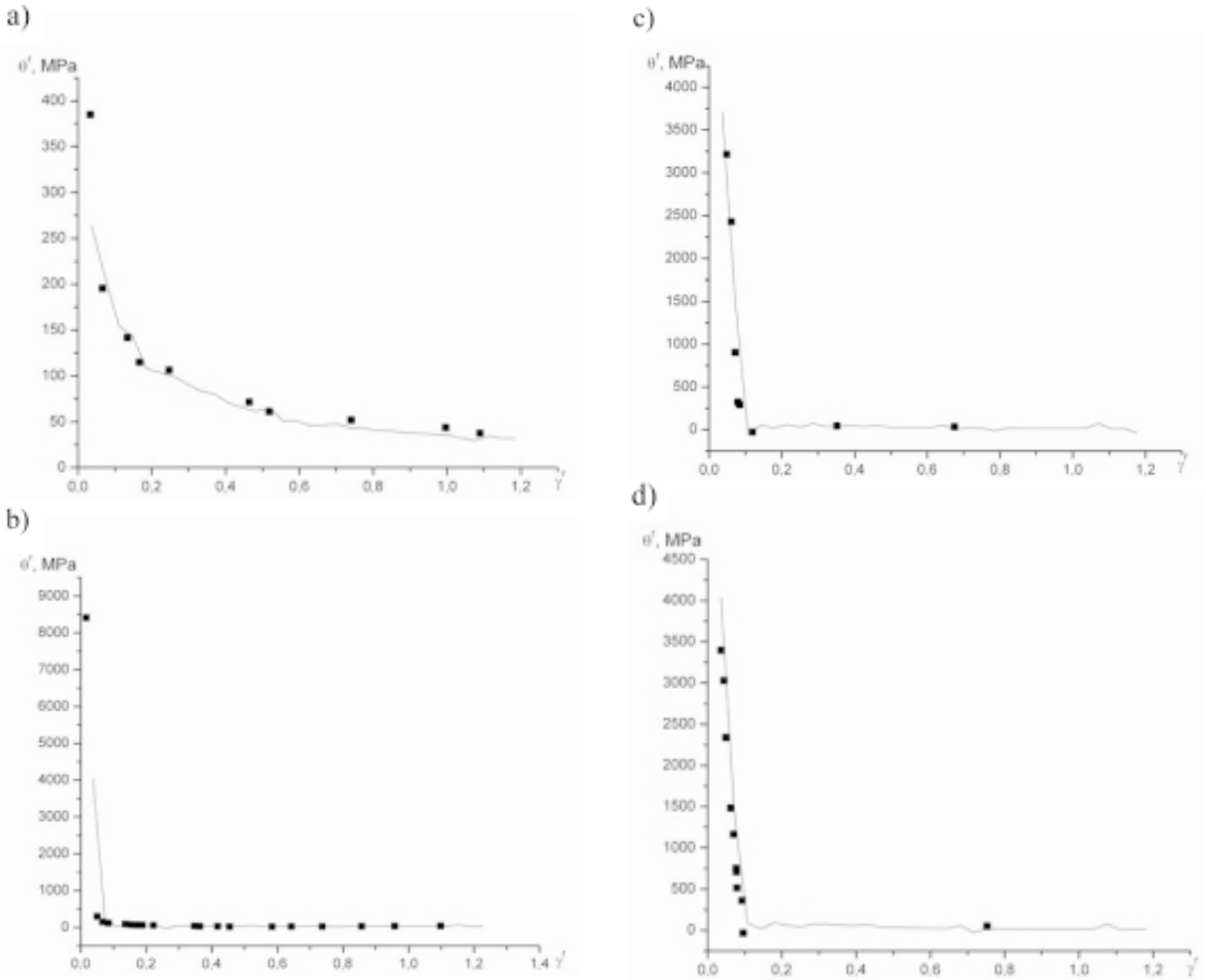

Fig. 6. Experimental (■) and modeling (-) hardening rate dependence of the resolved strain (evolution of the Taylor factor is taken into account): (a) initial state, after 1st (b), 4th (c), 8th (d) ECAP passes along B_c.

Table 3. The parameters, obtained during tensile strain of Cu in different structured states.

Parameters	As-received	1st pass route B_c	4th pass route B_c	8th pass route B_c
α^*	0.059	0.092	0.151	0.154
β^*	0.010	0.019	0.022	0.022
$\chi_a(0)$	4.2	10.7	15.7	15.3
K	10.00	8.00	6.0	6.0
C	$4.0\cdot10^{-6}$	$1.1\cdot10^{-2}$	70	300
$\widetilde{R}_f$	6.8	3.2	3.0	3.0
P_f	0.11	0.77	0.92	0.92
P_f'	0.35	0.17	0.050	0.001
M^*	2.47	2.48	2.38	2.39
f_0	0.250	0.145	0.066	0.060
α	0.36	0.46	0.42 ($0\le\gamma\le3.57\cdot10^{-2}$)	0.40 ($0\le\gamma\le3.58\cdot10^{-2}$)
			0.11 ($3.57\cdot10^{-2}<\gamma<0.11$)	0.38 ($3.57\cdot10^{-2}<\gamma<0.11$)
			$\gamma\ge0.11$	$\gamma\ge0.11$

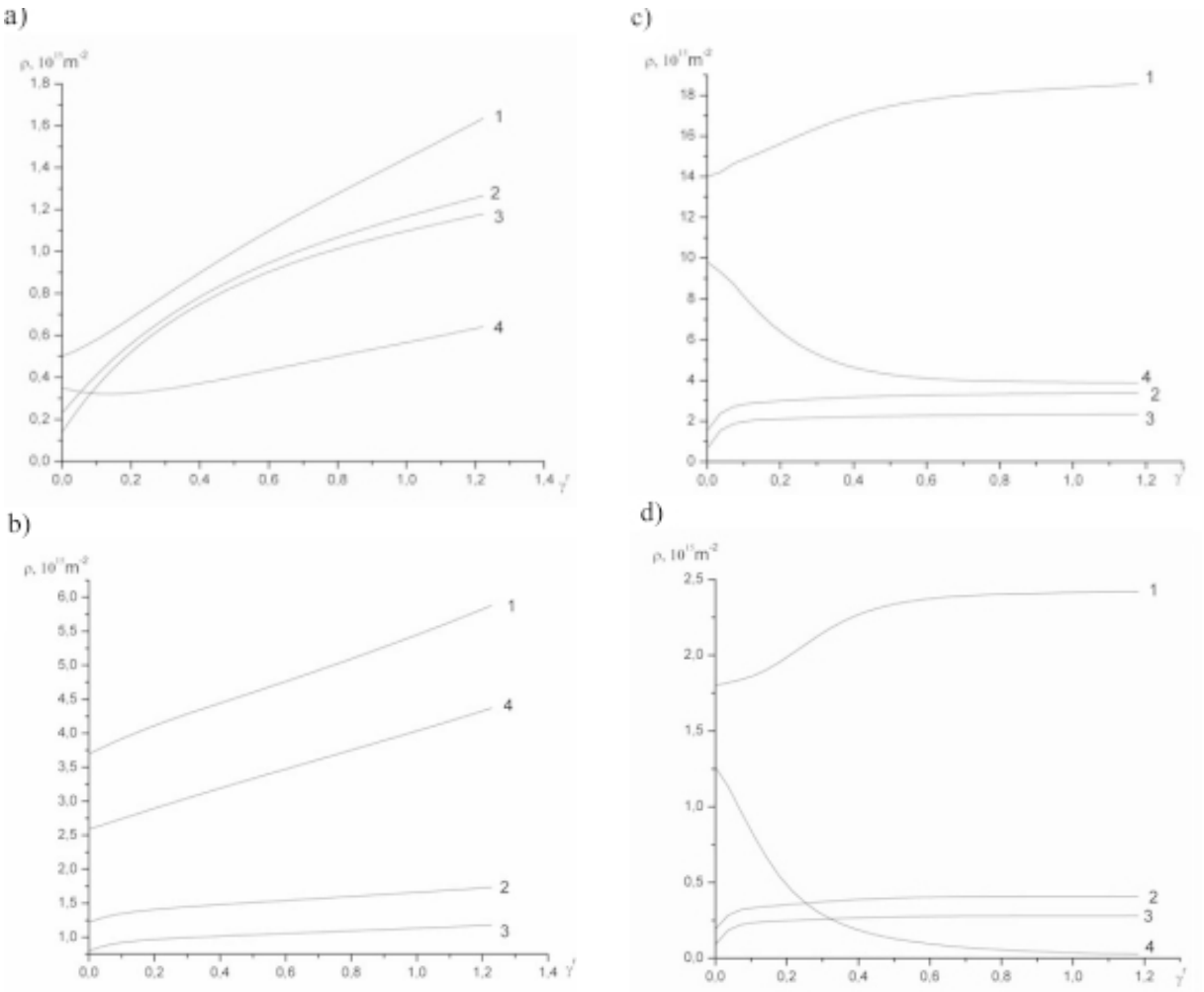

Fig. 7. Dislocation densities (1 – in the fragment boundaries, 2 – total, 3 – in the fragment interiors, 4 – of the non-excess sessile dislocations in the fragment boundaries) in Cu, depending on the resolved strain (evolution of the Taylor factor is considered) during tensile test from the initial state (a), after 1st (b), 4th (c), 8th (d) passes of ECA pressing along the route $3.57 \cdot 10^{-2}$.

samples in the above-mentioned states, their values are presented in Table 3. The values of the true stresses on the experimental curves were divided by the integral Taylor factor. The values of the true strain were multiplied by the integral Taylor factor.

The evolutions of the dislocation densities, namely, the total dislocation density ρ_{total}, the dislocation density in the fragment boundaries ρ_w, the dislocation density in the interiors ρ_c, the density of non-excess sessile dislocations ρ_j in the fragment boundaries, were predicted with the help of the dislocation model of a composite sample. Fig. 7 shows the dislocation densities - averaged sum of crystallographic shears graphs. Fig. 8 presents the experimental values of the dislocation density from [24].

As seen from Table 3, the tension after the 1st, 4th, and 8th ECAP passes is accompanied by the increase of activity of the sources in the fragment boundaries, which is characterized by the parameter α^*, in comparison with the sample deformed in the as-received state. It may be explained by the fact that the piling-up of dislocations has already occurred during ECAP and that results in the growth of internal stresses necessary for the subsequent deformation; therefore, the number of active sources increases. For example, simulations show that the total dislocation density is almost 3.8 times higher during tension after the 8th ECAP pass

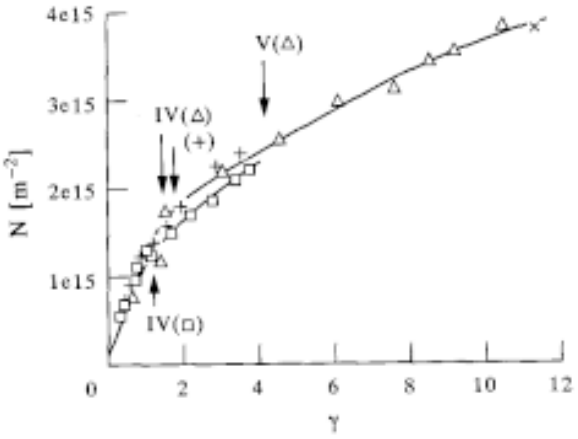

Fig. 8. Evolution of dislocation density N during high pressure torsion (+), rolling (▽), upsetting (□) with the rate $\dot{\gamma}=10^{-2}\cdot s^{-1}$ [24].

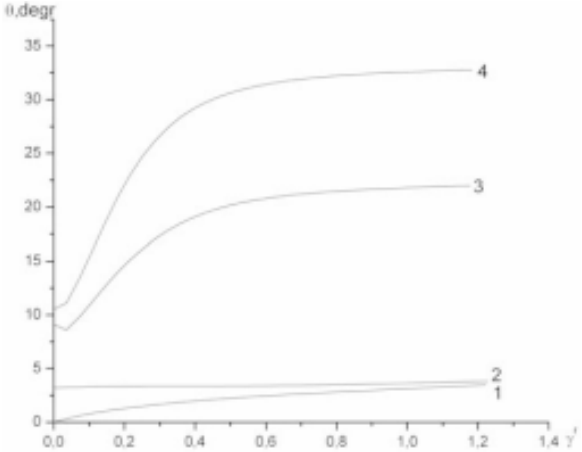

Fig. 9. Evolution of misorientations during tension of Cu depending on the resolved shear stress: 1 – as-received, 2, 3, 4 - after 1st, 4th, and 8th ECAP passes along the route B_c, respectively.

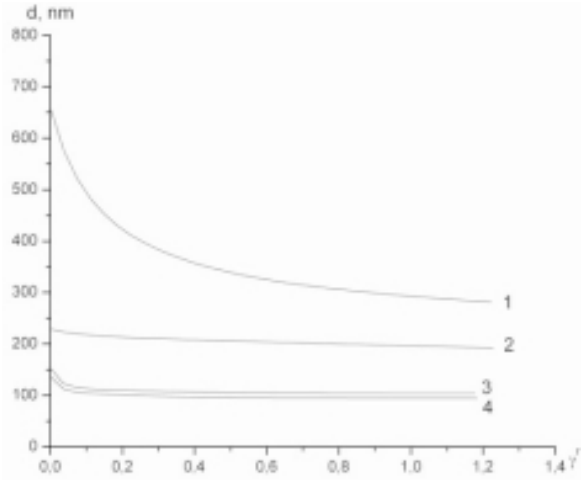

Fig. 10. Evolution of the fragment sizes during tension of Cu: 1 – as-received, 2, 3, 4 - after 1st, 4th, and 8th ECAP passes along the route B_c.

than during tension of the as-received Cu for the strain degree $\gamma = 0{,}8$. Activation of Frank-Read sources in the boundaries results in growth of the coefficient α^*. As a result, the flux of dislocations, which come into the interiors from the boundaries, also grows. The increase of the coefficient β^* characterizes the activation of dislocation absorption by the fragment boundaries.

The dislocation density grows in the boundaries with the strain degree rising in all considered cases. The growth of the dislocation density in the fragment boundaries leads to some qualitative changes in their structure [50]; we also observed this phenomenon after the conducted simulation. At that, the increase of misorientations is 6 and 9 times higher (with respect to the as-received state during the deformation after the 4th and 8th passing along the route B_c) than during the deformation of the as-received Cu. Misorientations during the deformation of Cu after the 1st pass along the route B_c are almost the same as during deformation of the as-received Cu (Fig. 9).

The density of non-excess sessile dislocations in the boundaries decreases with the strain degree rising during the tension of samples after 4th and 8th passes. This testifies to the activation of diffusional processes in the boundaries, annihilation of dislocations of opposite signs during capture, and decrease of the fraction of non-excess sessile dislocations in the boundaries, which is reflected in the reduction of the parameter P_f' values. As the total dislocation density in the boundaries grows, the decrease of the density of non-excess sessile dislocations is accompanied by the growth of the excess dislocation density and, therefore, by the density of misorientations between fragments (Fig. 8).

The non-excess sessile dislocation density grows with the strain rising in case of Cu at the initial state and after the 1st ECAP pass. This is connected with the slightly-expressed diffusional processes and low rates of dislocation climbing, which are conditioned by smaller values of the corresponding stress deviator tensor component and, therefore, by the slight annihilation during capture. In the given case, the value of the parameter P_f'

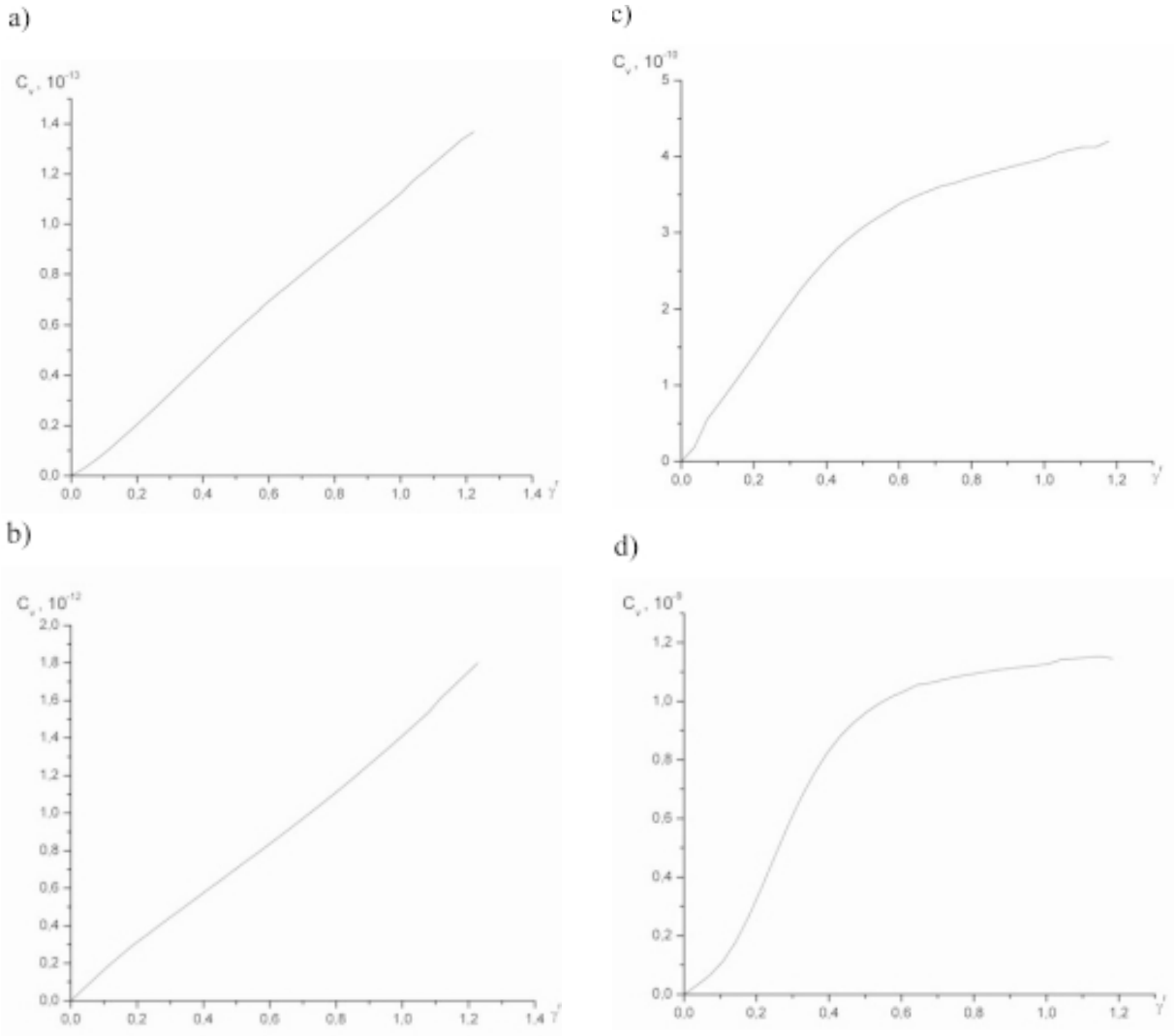

Fig. 11. Concentration of vacancies in Cu as-received (à), after 1st (b), 4th (c), and 8th (d) ECAP passes along the route B_c.

that controls the fraction of non-excess sessile dislocations is higher. The fraction of excess dislocations is lower and, therefore, misorientations between the fragments are smaller (Fig. 8). The fragment boundaries are less perfect and their structure is less ordered. This is also evidenced by the parameter P_f which characterizes permeability of boundaries.

The fragment sizes reduce during tension of samples in the as-received state and after the 1st , 4th, and 8th ECAP passes. During tension after the 1st pass the fragment sizes are about 200 nm, after the 4th pass they are about 100 nm, and after the 8th pass they become less than 100 nm (Fig. 10). Fragment sizes reduce more intensively before the 4th pass, while misorientations between the fragments increase (Fig. 9) at insignificant change of their sizes after the 4th pass. This agrees with the experimental data [30].

Severe plastic deformation delivers many lattice defects and vacancies [24,27,51]. Fig. 11 presents the vacancy concentration - strain degree graphs for Cu in the initial state and after the 1st, 4th, and 8th ECAP passes along the route B_c. The concentration of deformation vacancies reveals a dramatic growth when the number of ECAP passes increases. The equi-axed vacancy concentration is about 10^{-20} at room temperature [24], this value

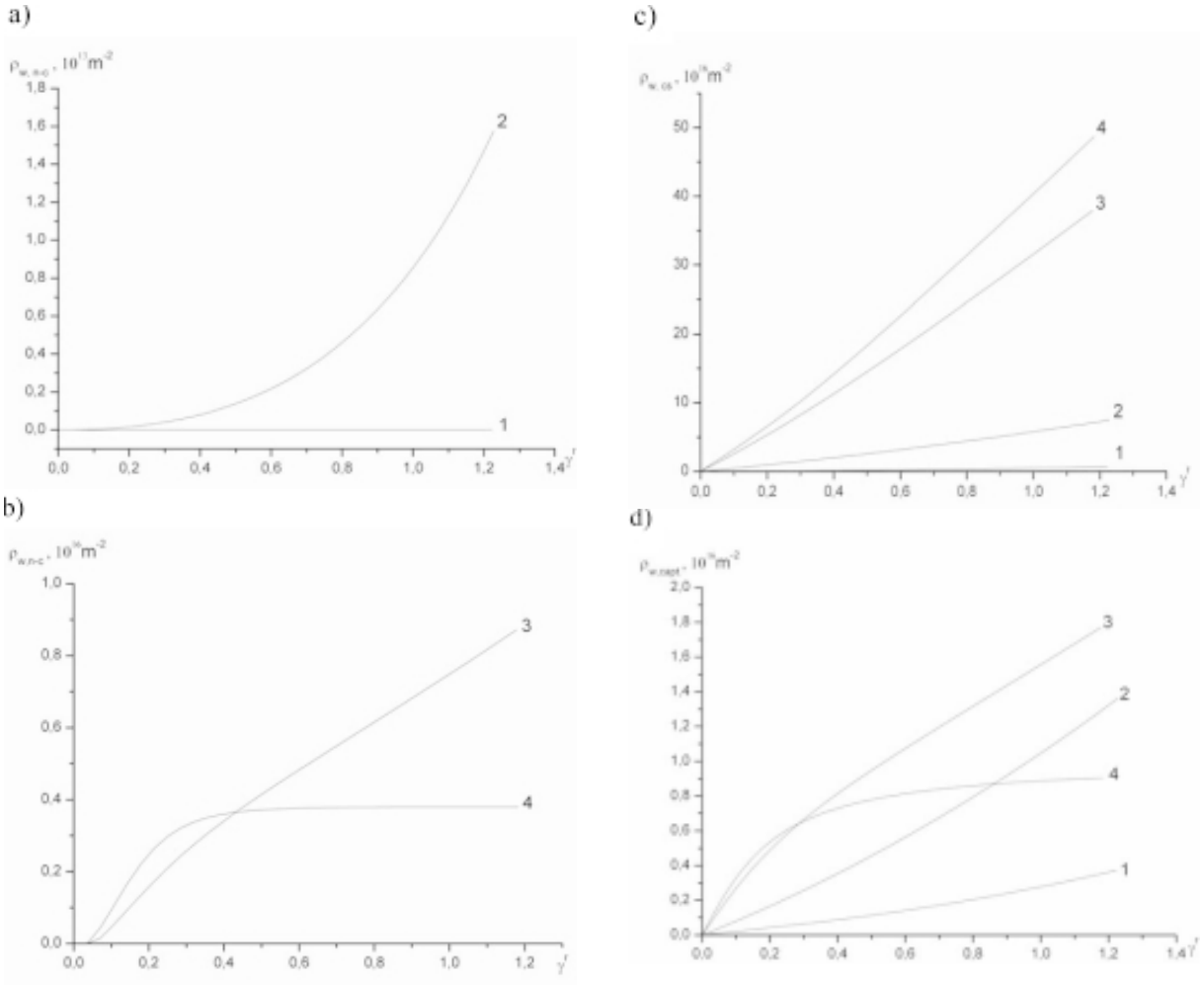

Fig. 12. Evolution of the dislocation densities, described by the corresponding members of Eq. (29), in the fragment boundaries as a result of non-conservative motion of dislocations $\rho_{w,\,n\text{-}c}$(*a*) ,$\rho_{w,\,n\text{-}c}$(*b*); of annihilation as a result of double cross slip $\rho_{w,\,cs}$(*c*); of capture of edge dislocations $\rho_{w,\,capt}$(*d*) in Cu during tension of samples, taken as-received (1), after 1st (2), 4th (3) and 8th (4) ECAP passes along the route B_c.

in Cu increases by 11 orders after the 8th pass. The concentration of deformation vacancies in Cu after the 8th pass is 4 orders higher than that in the as-received Cu. These data coincide with the results received in [43].

Figs. 12a and 12b shows the evolution of the dislocation density (in the non-dimensional variables) in the fragment boundaries at the expense of the diffusion-conditioned annihilation processes. In case of Cu after the 8th ECAP pass, annihilation during deformation turns is restricted and the density of annihilating dislocations decreases (Fig. 12b). As a result, the dislocation density in the boundaries and the total dislocation density grow. At that, the vacancy concentration increases (Fig. 11). This can be explained by obstructivity for vacancy diffusion with the increase in the number of passes.

Annihilation during the non-conservative motion of dislocations contributes significantly to the recovery process being responsible for the growth of misorientations between the fragments.

The density of dislocations which annihilate as a result of double cross slip in the fragment boundaries increases in all considered structure states of Cu (Fig. 12c).

The growth in density of the dislocations which annihilated during capture of edge dislocations of

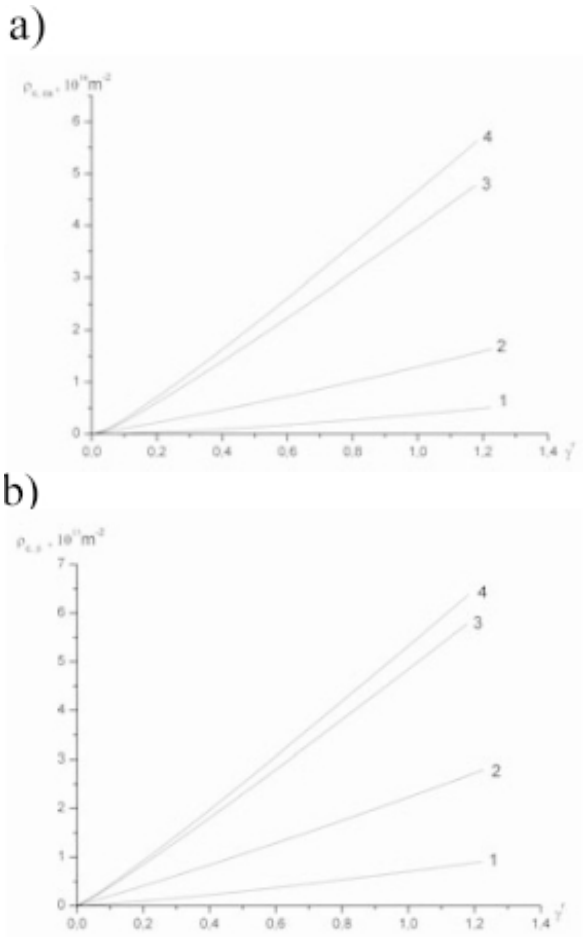

Fig. 13. Evolution of the dislocation densities, described by the corresponding members of Eq. (32), in the fragment interiors during the annihilation of dislocations as a result of double cross slip $\rho_{c,cs}$(*a*); coming from the internal areas into the fragment boundaries $\rho_{c,\beta}$(*b*) during tension of Cu samples, taken (1) as-received, after 1st (2), 4th (3), and 8th (4) ECAP passes.

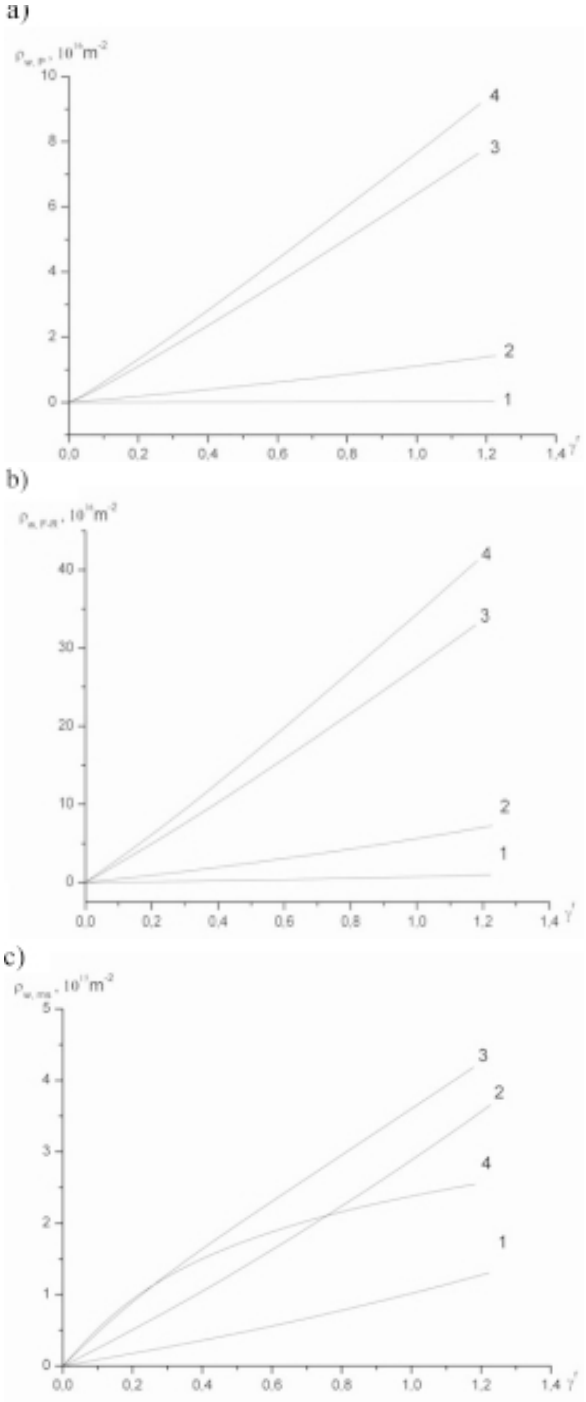

Fig. 14. Evolution of the dislocation densities, described by the corresponding member of Eq. (29), in the fragment boundaries as a result of immobilization of dislocations coming from interiors $\rho_{w,p}$(*a*); of activation of Frank-Read sources $\rho_{w,F\text{-}R}$(*b*); of dislocation generation during multiple slip $\rho_{w,ms}$(*c*) during tension of Cu samples, taken as-received (1), after 1st (2), 4th (3), and 8th (4) ECAP passes.

opposite signs is restricted after the 8th ECAP pass. That results in the increase of the dislocation density in the boundaries and the total dislocation density (Fig. 12d).

The density of the dislocations which annihilated as a result of double cross slip in the fragment interiors grows with the degree of the accumulated strain rising (Fig. 13a). The density of dislocations leaving the interiors also grows with the degree of the accumulated strain rising (Fig. 13b).

When the strain degree grows, the density of dislocations in the boundaries increases as a re-

sult of immobilization of the dislocations which come from interiors (Fig. 14a) and activation of Frank-Read sources (Fig. 14b). The increase in the dislocation density during multiple slip is restricted in Cu after the 8th ECAP pass. This can be explained by a decrease in the density of non-excess sessile dislocations (Fig. 14c). The growth of the dislocation density in the interiors is conditioned by the influence of the Frank-Read sources (Fig. 15a) and dislocation generation during multiple slip (Fig. 15b).

The results of the conducted modeling exhibit a significant influence of ECA pressing on the structure and processes which take place during tension of Cu taken in different structural states. The coefficient α^* characterizes the effectiveness of the Frank-Read sources, which are superficial for the fragment interiors. This coefficient increases 2.6 times after the 8th ECAP pass in comparison with the as-received Cu. The dislocation sink coefficient β^* increases 2.2 times. The boundaries absorb dislocations which come from the interiors. The annihilation coefficient $\chi_a(0)$ in the samples subjected to SPD is 10.7 after the 1st pass, 15.7, and 15.3 after 4th and 8th passes, respectively; this corresponds to the values typical for the conditions of hydrostatic pressures [40]. The annihilation coefficient is χ_a=2÷10 under the usual conditions of fcc metals deformation at moderate temperatures, while χ_a = 4.2 for the as-received Cu grade used in this paper.

The value of the parameter *K* which characterizes the fragment sizes does not change after the 4th ECAP pass. Therefore, the fragment sizes (Fig.10) after the 4th ECAP pass do not change significantly. Structure refinement generally takes place before the 4th pass of ECAP.

The parameter *C* that controls intensity of the growth of vacancy concentration increases with the degree of the accumulated strain rising. The annihilation length decreases before the 4th pass, after that it remains constant and equals to 3.

The boundaries are practically impermeable after the 4th pass. The parameter P_f that characterizes the fraction of the dislocations immobilized in the boundaries increases with the degree of the accumulated strain rising; after the 4th pass it remains unchanged. The value of the parameter is about 8.4 times higher after the 8th ECAP pass than that in the initial state.

The parameter P_f' that reflects the fraction of non-excess sessile dislocations in the boundaries decreases 350 times in comparison with its value

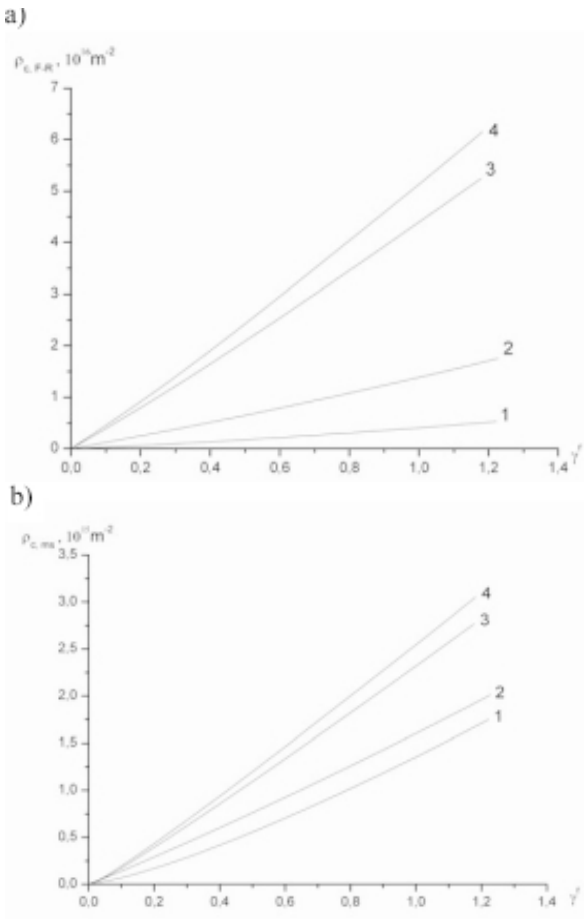

Fig. 15. Evolution of the dislocation densities, described by the corresponding member of Eq. (32), in the fragment interiors as a result of activation of Frank-Read sources $\rho_{c,\,F\text{-}R}(a)$; of dislocation generation during multiple slip $\rho_{c,\,ms}(b)$ during tension of Cu samples, taken as-received (1), after 1st (2), 4th (3), and 8th (4) ECAP passes.

for the as-received Cu. This testifies to the fact that after the 4th ECAP pass insignificant structure refinement takes place, but the process of boundary improvement occurs, i.e. the boundaries become more ordered. Misorientations between the fragments increase. The fraction of dislocations, which become non-excess sessile ones, is 50 times lower after the 8th ECAP pass than after the 4th pass. The density of non-excess sessile dislocations decreases, and, therefore, the annihilation of dislocations during capture in the boundaries and dislocation generation on the “forest” dislocations reduce.

The vacancy concentration continues increasing. Diffusion processes slow down after the 8th ECAP pass, so that annihilation of dislocations in the fragment boundaries decreases during their non-conservative motion.

Thus, we may conclude that the structure of fragment boundaries after 8 ECAP passes is of different quality. They are highly-misoriented. The fraction of non-excess sessile dislocations is negligibly small. Misorientations between fragments are high.

7. CONCLUSIONS

1. The presented model consistently describes the observed experimental data.
2. The presented model allows describing quantitatively the dependency of the dislocation density on the number of passes along the given ECAP route.
3. The study of the evolution of the dislocation density as a result of influence of different mechanisms has shown that the role of annihilation processes, conditioned by capture and non-conservative motion of edge dislocations, is reduced after the 8th ECAP pass; the mechanism of dislocation generation is suppressed on the "forest" of dislocations. The mentioned changes reflect qualitative reconstructions in the structure of fragment boundaries. The boundaries become practically impermeable and the fraction of non-excess sessile dislocations is negligibly small.
4. Structure refinement takes place mainly up to the 4th ECAP pass. Upon that, misorientations between fragments remain low.
5. Misorientations between the fragments start to grow at minor changes of their sizes after the 4th ECAP pass.
6. The dramatic growth of vacancy concentration takes place with the number of passes increasing. At that, the dislocation density in the fragment boundaries and the total dislocation density grow.
7. The model predicts the evolution of vacancy concentration in the fragment boundaries and allows estimating their role in strain hardening and character of the forming fragment boundaries.
8. Insignificant strain hardening of the materials subjected to ECAP is explained by the fact that growth of the sources' activity is compensated by enhancement of annihilation processes. The contribution of each process can be estimated.
9. Considerable increase in the yield stress of the samples after the 1st, 4th, and 8th ECAP passes is explained by an increase in the dislocation density during ECAP.

REFERENCES

[1] Ya.M. Vitorskiy, E.Yu. Zubets, S.N. Kaverina, V.A. Manilov, V.I. Trefilov and V.I. Firstov // *Physics of Metals and Metallurgy* **33** (1972) 831.

[2] V.M. Bykov, V.A. Likhachev, Yu.A. Nikonov, L.L. Serbina and L.I. Shibalova // *Physics of Metals and Metallurgy* **45** (1978) 163.

[3] V.V. Rybin, *Large plastic deformations and failure of metals* (Metallurgia, Moscow, 1986).

[4] R.Z. Valiev and I.V. Alexandrov, *Nanostructured materials, processed by severe plastic deformation* (Logos, Moscow, 2000).

[5] R.Z. Valiev, I.V. Alexandrov, Y.T. Zhu and T.C. Lowe // *J. Mater. Res.* **17** (2002) 5.

[6] G.T. Gray III, T.C. Lowe, C.M. Cady, R.Z. Valiev and I.V. Alexandrov // *Nanostr. Mater.* **9** (1997) 477.

[7] R.Z. Valiev, R.K. Islamgaliev and I.V. Alexandrov // *Progr. Mater. Sci.* **45** (2000) 103.

[8] V.Yu. Gertsman, R.Z. Valiev, N.A. Akhmadeev and O. Mishin // *Mater. Sci. Forum*. **233** (1996) 749.

[9] R.Z. Valiev and R.K. Islamgaliev // *Physics of Metals and Metallurgy* **85** (1998) 161.

[10] R.Z. Valiev, E.V. Kozlov, Yu.F. Ivanov, J. Lian, A.A. Nazarov and B. Baudelet // *Acta Metall. Mater.* **42** (1994) 2467.

[11] T. Ungár, In: *Proceedings of the NATO Advanced Research Workshop on Investigations and Applications of Severe Plastic Deformation*, ed. by T.C. Lowe and R.Z. Valiev (Kluwer Academic Publishers, Dordrecht-Boston-London, 2000), p. 93.

[12] A.A. Popov, R.Z. Valiev, I.Yu. Pyshmintsev, S.L. Demakov and A.G. Illarionov // *Physics of Metals and Metallurgy* **83** (1997) 127.

[13] R.K. Islamgaliev, D.A. Salimonenko, L.O. Shestakova and R.Z. Valiev // *Izvestiya Vuzov. Tsvetnaya Metallurgia* **6** (1997) 52.

[14] Yu.R. Kolobov, R.Z. Valiev and G.P. Grabovetskaya, *Grain boundary diffusion and properties of nanostructured materials* (Nauka, Novosibirsk, 2001).

[15] G.A. Malygin // *Solid State Physics*. **29** (1987) 2067.

[16] J. Lian, B. Baudelet and A.A. Nazarov // *Mater. Sci. Engin*. **A172** (1993) 23.
[17] V.Y. Gertsman, R. Birringer, R.Z. Valiev and H. Gleiter // *Scripta Metall. Mater.* **30** (1994) 229.
[18] Y. Estrin and H. Mecking // *Acta Metall.* **32** (1984) 57.
[19] H. Mecking and U.F. Kocks // *Acta Metall.* **29** (1981) 1865.
[20] S. Kok, A.J. Beaudoin and D.A. Tortorelly // *Acta Mater.* **50** (2002) 1653.
[21] Y. Estrin, L.S. Tóth, A. Molinari and Y. Bréchet // *Acta Mater*. **46** (1998) 5509.
[22] E. Nes and K. Marthinsen // *Mater. Sci. Engin.* **A322** (2002) 176.
[23] E. Nes // *Progr. Mater. Sci.* **41** (1998) 129.
[24] M. Zehetbauer // *Acta Mater.* **41** (1993) 589.
[25] P. Les and M. Zehetbauer // *Key Eng. Mater.* **97-98** (1994) 335.
[26] H. Mughrabi // *Acta Metal.* **31** (1983) 1367.
[27] M. Zehetbauer and V. Seumer // *Acta Metall. Mater.* **41** (1993) 577.
[28] L.S. Tóth, A. Molinari and Y. Estrin // *J. Eng. Mater. Technol.* **124** (2002) 71.
[29] U.F. Kocks, C.N. Tomé and H.-R. Wenk. *Texture and Anisotropy* (2nd edition, Cambridge Univ. Press, Cambridge, 2000).
[30] S.C. Baik, R.J. Hellmig, Y. Estrin and H.S. Kim // *Z. Metallkd.* **94** (2003) 754.
[31] V. Yamakov, D. Wolf, S.R. Phillpot, A.K. Mukherjee and H. Gleiter // *Nat. Mater*. **1** (2002) 45.
[32] X.Z. Liao, Y.H. Zhao, S.G. Srinivasan, Y.T. Zhu, R.Z. Valiev and D.V. Gunderov // *Appl. Phys. Lett.* **84** (2004) 592.
[33] R.J. Asaro, P. Krysl and B. Kad // *Phil. Mag. Lett*. **83** (2003) 733.
[34] Y.T. Zhu, X.Z. Liao, S.G. Srinivasan and E.J. Lavernia // *Journal of Appl. Phys.* **98** (2005) 034319.
[35] S.V. Bobylev, M.Yu. Gutkin and I.A. Ovidko // *Fizika Tverdogo Tela* **48** (2006) 1410.
[36] A.N. Vergazov, V.A. Likhachev and V.V. Rybin // *Physics of Metals and Metallurgy.* **42** (1976) 1241.
[37] D.A. Hughes and N. Hansen // *Acta Mater.* **45** (1997) 3871.
[38] L.E. Popov, V.C. Kobytev and T.A. Kovalevskaya, *Plastic deformation of the alloys* (Metallurgia, Moscow, 1984).
[39] G.A. Malygin // *Physics of Solid State.* **29** (1987) 2067.
[40] G.A. Malygin // *Physics of Solid State.* **32** (1992) 3200.
[41] P.I. Polukhin, S.S. Gorelik and V.K. Vorontsov, *Principal physics of plastic deformation* (Metallurgia, Moscow, 1982).
[42] U. Essman and H. Mughrabi // *Phil. Mag.* **A40** (1979) 731.
[43] M.J. Zehetbauer, H.P. Stüwe, A. Vorhauer, E. Schafler and J. Kohout // *Adv. Engin. Mater*. **5** (2003) 330.
[44] F.B. Prinz and A.S. Argon // *Acta Metall.* **32** (1984) 1021.
[45] G.A. Malygin // *Physics of Solid State*. **34** (1992) 2882.
[46] W. Pantleon // *Acta Mater.* **46** (1998) 451.
[47] C.N. Tomé // *Mod. Sim. Mats. Sci. Eng.* **7** (1999) 723.
[48] V.M. Segal // *Mat. Sci. Engin*. **A197** (1995) 157.
[49] T. Ungár, I. Alexandrov and P. Hanák, In: *Proceedings of the NATO Advanced Research Workshop on Investigations and Applications of Severe Plastic Deformation*, ed. by T.C. Lowe and R.Z. Valiev (Kluwer Academic Publishers, Dordrecht-Boston-London, 2000), p. 133.
[50] M. Zehetbauer, E. Schafler, T. Ungár, S. Kopacz and S. Bernstorf // *ASME J. Eng. Mater. Technol.* **124** (2002) 41.
[51] B.B. Straumal, B. Baretzky and A.A. Mazilkin // *Acta Mater.* **52** (2004) 4469.